Measurement report: Atmospheric CH₄ at regional stations of the Korea Meteorological Administration/ Global Atmosphere Watch Programme: measurement, characteristics, and long-term changes of its drivers

Haeyoung Lee[1, 2*], Wonick Seo[1], Shanlan Li[1], Soojeong Lee[1], Samuel Takele Kenea[1], and Sangwon Joo[1]

[1] National Institute of Meteorological Sciences, Jeju, 63568, Republic of Korea
[2] Tropospheric Chemistry, National Institute of Water and Atmospheric Research (NIWA), Wellington, New Zealand

Correspondence to Haeyoung Lee (Haeyoung.Lee@niwa.co.nz or leehy80@korea.kr)

Abstract. To quantify CH₄ emissions at policy-relevant spatial scales, the Korea Meteorological Administration (KMA) started monitoring its atmospheric levels in 1999 at Anmyeondo (AMY) and expanded monitoring to Jeju Gosan Suwolbong (JGS) and Ulleungdo (ULD) in 2012. The monitoring system consists of a Cavity Ring Down Spectrometer (CRDS) and a new cryogenic drying method, with a measurement uncertainty (68% c.i.) of 0.7–0.8 ppb. To determine the regional characteristics of CH₄ at each KMA station, we assessed the CH₄ level relative to local background (CH₄xs), analyzed local surface winds and CH₄ with bivariate polar plots, and investigated CH₄ diurnal cycles. We also compared the CH₄ levels measured at KMA stations with those measured at the Mt. Waliguan (WLG) station in China and Ryori (RYO) station in Japan. CH₄xs followed the order AMY (55.3±37.7 ppb) > JGS (24.1±10.2 ppb) > ULD (7.4±3.9 ppb). Although CH₄ was observed in well mixed air at AMY, it was higher than at other KMA stations, indicating that it was affected not only by local sources but also by distant air masses. Annual mean CH₄ was highest at AMY among all East Asian stations, while its seasonal amplitude was smaller than at JGS, which was strongly affected in the summer by local biogenic activities. From the long-term records at AMY, we confirmed that growth rate increased by 3.3 ppb·yr⁻¹ during 2006/2010 and by 8.3 ppb·yr⁻¹ from 2016 to 2020, which is similar to the global trend. Studies indicated that the recent global accelerated CH₄ growth rate was related to biogenic sources. However, $\delta^{13}CH_4$ indicate that the CH₄ trend in East Asia is derived from biogenic and fossil fuel sources from 2006 to 2020. We confirmed that long-term high-quality data can help understand changes in CH₄ emissions in East Asia.

1.   Introduction

Atmospheric methane (CH₄) is an important greenhouse gas and is one of the main drivers of climate change. The global atmospheric CH₄ abundance was 1889±2 ppb in 2020, increasing 2.6 times since 1750 (~722 ppb, pre-industrial period); the relative CH₄ increase since pre-industrial is greater than other major greenhouse gases such as CO₂ (1.5 times) and nitrous oxide (1.2 times) (WMO, 2021). Recently, CH₄ has gained substantial interest because of its relatively shorter lifetime in the atmosphere (~ 9 year) compared with those of other long-lived greenhouse gases (Prinn et al., 2005). CH₄ emission reduction may thus be an effective method to partially mitigate climate change. The 6th Intergovernmental Panel on Climate Change (IPCC) reported that, if

strong and sustained CH$_4$ emission reductions are integrated with air pollution controls, net warming could decrease in the long term because of the short lifetime of both CH$_4$ and aerosols (IPCC, 2021).

To reduce the atmospheric CH$_4$ burden, its emissions and sinks must first be quantified. CH$_4$ loss is primarily attributed to reaction with hydroxyl radicals (OH), which are part of atmospheric photochemical cycles, while there are various natural (wetlands, freshwaters, and geological) and anthropogenic CH$_4$ sources (agriculture, waste, fossil fuels, and biomass burning) with different spatial and temporal distributions (Lan et al., 2021, Basu et al., 2022). Because of its diverse sources in different regions, high resolution, quality data can help quantify the atmospheric CH$_4$ budget.

In the World Meteorological Organization (WMO), Global Atmosphere Watch Programme (GAW), there are 170 stations that monitor atmospheric CH$_4$, but with poor spatial coverage in Asia (gawsis.meteoswiss.ch, last access: November 2021).

Among CH$_4$ sources, rice agriculture is intense in Asia, mainly in China and India (Kai et al., 2011). China has also the largest anthropogenic CH$_4$ emissions in the world mainly from solid fuel (34%), rice cultivations (20%) and enteric fermentation (10%), (Janssens-Maenhout et al., 2019; Crippa et al., 2022). South Korea ranks among the world's top three importers of liquefied natural gas (LNG), following Japan and China (eia.gov/international/analysis/country/KOR. last access: November 2021). South Korea major CH$_4$ emissions are derived from wastewater treatment (40%), enteric fermentation (22%) and then rice cultivations (14%) (Crippa et al., 2022). In this regard, the Korean atmospheric monitoring network is important to understand not only South Korea CH$_4$ flux but also the Asian continent, as it is sensitive to air masses transported from Asia, and especially from China.

South Korea's atmospheric CH$_4$ monitoring history started at Tae-Ahn Peninsula (TAP, 36.74°N, 126.13°E, 20 m above sea level) by Korea Centre for Atmospheric Environment Research in the western part of Korea in 1990, with weekly flask-air sample collection as a part of the U.S. National Oceanic and Atmospheric Administration (NOAA), Global Monitoring Laboratory (GML), Cooperative Global Air Sampling Network (http://www.esrl.noaa.gov/gmd/ccgg/flask.php). Since 1999, the Korea Meteorological Administration (KMA) has been monitoring atmospheric CH$_4$ with quasi-continuous measurements at Anmyeondo (AMY, 36.53°N, 126.32°E, a 40 m tower whose base is 46 m above sea level), approximately 28 km from TAP. In 2012, KMA expanded its monitoring network to capture data from the south-west (Jeju Gosan Suwolbong, JGS, 33.30°N, 126.16°E) and east (Ulleungdo, ULD, 37.48°N, 130.90°E) of Korea to cover the entire peninsula for a better understanding of CH$_4$ sources and their characteristics. However, there is no published description of measurement quality, regional characteristics and long-term trends of CH$_4$ for Korea network.

A few studies reported that CH$_4$ levels are affected by emissions from Russian wetlands and local rice cultivation near TAP (Dlugokencky et al., 1993; Kim et al., 2015). In 2019, observations at AMY indicate larger emissions compared with previous years, which were caused by soil temperature and moisture changes (Kenea et al., 2021). In summer, high atmospheric CH$_4$ levels were observed in airborne measurements because of biogenic sources such as rice paddies, landfills, and livestock (Li et al., 2020). The observed atmospheric ratio, CH$_4$/C$_2$H$_6$, was 53 ppb·ppb^{-1} during KORUS-AQ campaign from May to June 2016 which is related to fossil fuel use in Seoul and Busan while it was 150 to 250 ppb·ppb^{-1} in southwestern South Korea related to biogenic emissions such as rice paddies(Li et al., 2022). These studies indicate CH$_4$ emissions sources are diverse in Korea based on short-term campaign study. Therefore, it can be difficult to figure out the representative long-term and regional characteristics in Korea. Also, even if CH$_4$ is monitored long-term at regional scale, poor measurement quality can lead to misinterpretation of the CH$_4$ budget, preventing development of science-based policies. Additionally, both measurement uncertainty and inadequate assessment of background air can limit the accuracy of observation-based estimates for local or regional scale greenhouse gas emissions (Graven et al., 2012; Turnbull et al., 2009, 2015; Lee et al., 2019).

In this paper, we present CH$_4$ data quality procedures and processing methods at three KMA monitoring stations, including measurement uncertainties. We analyzed the characteristics of CH$_4$ at the KMA stations from 2016 to 2020 and compared the data with those collected at other stations in East Asia: the global background WMO/GAW station in Waliguan (WLG, 36.28°N, 100.90°E, 3810 m), China; and the WMO/GAW station at Ryori (RYO, 39.03°N, 141.82°E, 260 m) in Japan, which reflects the global growth rate (Watanabe et al., 2000). In addition, we investigated the changes in CH$_4$ enhancement from 2006 to 2020 and analyzed source regions based on measurements of $\delta^{13}C_{(CH4)}$ in flask-air samples to trace the major source changes. Furthermore, this study can serve as a reference for KMA data archived at the World Data Centre for Greenhouse Gases.

2.   Experiment

2.1   Sampling sites

The locations of AMY, JGS, and ULD stations are shown in Fig. 1 and summaries of the measurement systems are in Table 1. Detailed information was provided in Lee et al. (2019). Only key information focusing on CH$_4$ is summarized here.

AMY is located in the western part of Korea approximately 28 km south from TAP and 130 km southwest from the megacity of Seoul. Within 50 km of AMY, the second largest rice paddies and largest livestock industry of Korea are present. The largest coal and heavy oil-fired thermal power plants in Korea are within 35 km of this station, to the north-east and south-east, respectively, and the largest LNG power plant in Korea is 100 km to the north east of this station. The local region mainly consists of agricultural land growing rice, sweet potatoes, and onions, and the area is also known for its leisure opportunities during summer. The west and south sides of AMY are open to the sea, with a large tidal mudflat with many pine trees along the coast.

JGS is located in the western part of Jeju Island, which is the largest volcanic island (1,845.88 km^2) in the south-west of Korea and is approximately 90 km from the mainland. The major industries here are tourism and livestock, which focuses on horses and pigs. JGS is located within a famous Global Geo-park that has outcrops of volcanic deposits exposed along the coastal cliff. Next to JGS, agriculture is widespread, with potatoes, garlic, and onions being the main crops in the largest plain in Jeju Island. The station is open to the sea from the south-west to north-west, with the cliffs comprising volcanic basalt rocks. The sea to the south is connected to the East China Sea and the sea to the west is linked to the Yellow Sea.

ULD is located in the east of Ulleung Island, which is in the eastern part of Korea and approximately 155 km from the mainland. In the south-eastern part of the Korea Peninsula, numerous steel, chemical, and petrochemical industries are present along the coastline, within approximately 200–250 km from the island. There are two large natural gas power plants. Ulleung Island covers 72 km^2, and has a volcanic origin, being a rocky steep-sided island that is the top of a large stratovolcano that has a maximum elevation of 984 m. This peak is located northwest of ULD. There are a few small mountains with heights from 500 to 960 m a.s.l., within 5 km to the north and southeast of the station. Because of those geological features, ULD is mainly affected by airflow from over the hill to the southwest and by downslope winds from northeast. In the southwestern area, there is a small brickyard 200 m from the station and a garbage incinerator within 100 m. The garbage incineration facility was moved to the north side of island in December 2016. Therefore, many studies do not include the data before 2017. Farming and fishing industries are very active on the island, although there are no farms in the southern area. An automatic weather station (AWS) was installed at AMY near the air sampling inlet, and 10 m above the station at JGS and ULD, independent from the air inlet tower.

Figure 1. Locations of KMA CH$_4$ monitoring stations in Korea: Anmyeondo (AMY, 36.53°N, 126.32°E), Jejudo Gosan Suwolbong (JGS, 33.30°N, 126.16°E) and Ullengdo (ULD, 37.48°N, 130.90°E). Tae-an Peninsula (TAP, 36.74°N, 126.13°E), part of NOAA's flask-air sampling network, is 28 km from AMY in South Korea. Mt. Waliguan (WLG, 36.28°N, 100.90°E) and Ryori (RYO, 39.03°N, 141.82°E) are located in China and Japan, respectively. This map is derived from google map.

2.2   Measurement environment and instrument

At all three stations, the measurement system consists of 1) inlet, 2) pump, 3) drying system, and 4) analyzer. Detailed information of the system was discussed by Lee et al. (2019).

1) Inlet: Dekabon sampling tubing (Nitta Moore 1300-10, I.D. 6.8 mm, O.D. 10 mm, high-density polyethylene jacket, overlapped aluminum tape, and ethylene copolymer liner) with a stainless-steel filter (D 4.7 cm, pore size 5 µm) mounted on a plastic mesh holder   installed on the intake and connected to the pump. The inlet height was changed at AMY in 2004 and at JGS in 2017 (Table 1).

2) Pump: A KNF diaphragm pump (N145.1.2AN.18, Germany, 55 L/min, 7 bar in AMY; N035AN.18, Germany, 30 L/min, 4 bar in JGS and ULD) is installed between the inlet and drying system.

3) Drying system: Sample air is dried with a cryogenic method (CT-90, Operon, Korea). Inside the drying system, there are two chambers with two steps; ambient air is cooled to –20°C in the first chamber, and then to –50°C in the second chamber. This system was installed in 2012 at all three KMA stations. This system dried the sampled air enough so that the bias from the humidity is negligible. This is described in section 2.3 and 3.1.

4) Analyzer: A model G2301 (Picarro, USA) was installed in October 2011, and it became the official CH$_4$ measurement system at AMY starting February 1, 2016. Before February 2016 (G2301), a GC-FID was used to monitor atmospheric CH$_4$. CRDS records atmospheric CH$_4$ every 5 s across the KMA Greenhouse Gas (GHG) network while the GC-FID measured CH$_4$ every 30 min. At JGS, the monitoring of atmospheric CH$_4$ started with the use of G1301 in 2012, which was changed to G2401 from 2020. G2401 has been used from 2012 at ULD.

Table 1. Information on the three KMA CH_4 monitoring stations in Korea

Station (ID)	Longitude Latitude Altitude	Inlet height (period)	Instrument Model (period)	Drying method (period)	Standard scale (period)
Anmyeondo (AMY)	126.32°E 36.53°N 47 m a.s.l	20 m (1999 to 2004)	GC-FID (1999 to 2016 Feb)	Three step dehumidification system 1) –4°C cold trap 2) Nafion™ 3) $Mg(ClO_4)_2$ (1999 to 2011)	KRISS (1999 to 2011)
		40 m (since 2004)	CRDS 2301 for CO_2 and CH_4 (2016 Feb to present)	Cryogenic system (since 2012)	WMO-X2004A (2012 to present)
Jejudo Gosan Suwolbong (JGS)	126.16°E 33.30°N 71.47 m a.s.l	6 m (2012 to 2017) 12 m (since 2017)	CRDS 1301 for CO_2 and CH_4 (2012 to 2019) CRDS 2401 for CO_2, CH_4, and CO (since 2020)	Cryogenic system	WMO-X2004A (2012 to present)
Ulleungdo* (ULD)	130.90°E 37.48°N 220.9 m a.s.l	10 m (since 2012)	CRDS 2401 for CO_2, CH_4, and CO (since 2012)	Cryogenic system	WMO-X2004A (2012 to present)

*ULD is not registered in the GAW network.

2.3 Calibration method

Our highest-level standards are designated "laboratory standards". We have four laboratory standards prepared by the WMO GAW Central Calibration Laboratory (CCL) on the WMO-X2004A scale in the range 1700 to 2500 ppb with uncertainties of less than 2 ppb (95% confidence level, coverage factor k=2, gml.noaa.gov/ccl/ch4, last access: 5 Jan.,2023). They are provided in 29.5 L aluminum cylinders (Luxfer, UK) by the CCL   filled with 130 bar (https://gml.noaa.gov/ccl/services.html, last access: 5 Jan.,2023). Our laboratory standards have been recalibrated every 3 years or replaced with new sets since first use in 2012, according to GAW recommendations. Remaining pressure in each cylinder is still high,~100 bar.

For working standards, dry, ambient air is compressed into a cylinder at AMY with a range of roughly 1800-2500 ppb. To bracket the measurement range, we diluted collected air to around 1700 ppb with zero air.

Filled working standards are sent to a central laboratory of the National Institute of Meteorological Sciences (NIMS) in Jeju for calibration against the laboratory standards. The scale was transferred with a CRDS (G2401, Picarro, USA). The scale propagation uncertainty is described in section 3.1.

Normally the difference in H_2O between laboratory and working standards measured by CRDS is ~0.00054%, which leads to a bias of 0.01 to 0.014 ppb for CH_4 in the given range according to the Eq. (1) from Rella at al.(2013). This value is negligible, so it was not considered as a factor for the propagated uncertainty

$$\frac{C_{dilution}}{C_{dry}} = 1 - 0.01 H_{act} \qquad \text{(Eq. 1)}$$

where C is the CH_4 mole fraction and H_{act} is the water mole fraction difference between laboratory and standard gases (in %). For example, 0.00054% H_2O difference between two cylinders causes 0.01 ppb bias at 1800 ppb.

5 Analyzer response had been calibrated every two weeks for all stations before 2019 Dec. but it was changed to 5 or 6 days with different calibration frequency at each station based on the reproducibility; all 4 working standard gases with a range of 1700-2500 ppb at intervals of 200-300 ppb were measured by the CRDS for 40–50 min. Only the last 10 min of data were used for the calibration of CH_4 to ensure instrument stability (Lee et al., 2021). Our ability to maintain and propagate the WMO-2004A scale was shown through the 6th Round Robin comparison test (RR) of standards hosted by the CCL
10 (https://www.esrl.noaa.gov/gmd/ccgg/wmorr/wmorr_results.php, the difference for low CH_4 levels was 0.7±0.7 ppb while that for high CH_4 levels was 0.6 ± 0.7 ppb)
When we started monitoring atmospheric CH_4 at AMY in 1999, the GC-FID response was calibrated every 1.5 h with a 1-point calibration against the KRISS scale until February 2016. During this period, we used standards that were certified directly by KRISS without working standards. KRISS and WMO-2004A scales agreed well with a difference from -0.1 to 0.8 ppb
15 (gml.noaa.gov/webdata/ccgg/wmorr/rr5, last access: Jun 2022). WMO round robin comparison of standard scales (Round robin number 5) included measurements with our GC-FID; differences with the CCL were from –0.3 to 1.3 ppb in the range 1756 to 1819 ppb.

2.4   Data quality control/assurance process and baseline selection method

20 ### 2.4.1 Auto and manual quality control/assurance process

All data were collected and stored at NIMS in Jeju, South Korea. Raw data at 5 s intervals (L0 data) were processed as L1 data with 1) auto flagging and 2) manual flagging. Auto flagging involved 6 criteria, including instrument malfunction, instrument detection limit, and value outside the given calibration range. Manual flags were assigned by technicians at each station according to the logbook based on inlet filter exchange, diaphragm pump error, low flow rate, dehumidification system error, calibration
25 periods, experimental periods such as participation in comparison experiments, observatory environmental issue such as construction next to a station, extreme weather, or other issues related to the instrument. These codes refer to definitions by the World Data Centre for reactive gases and aerosols maintained by EBAS for the GAW Programme (http://www.nilu.no/projects/ccc/flags/flags.html, last access: 23 Aug. 2022) that were modified for the South Korea network. Data with flags were reviewed by scientists at NIMS, and only valid data were averaged into Level 2 (L2) hourly average data. To define
30 valid data, all data were compared between South Korea stations and other global stations at similar latitude to Korea.
One of the ways of quality assurance, a co-located comparison of discrete samples collected at AMY, the sampled flasks were analyzed by NOAA/GML and compared with our in-situ analyzer results. This comparison between L2 hourly data from the CRDS and weekly flask-air samples collected at AMY has been ongoing since December 2013. The mean difference, flask minus CRDS hourly mean in situ, was 2.2 ± 11.8 ppb from 2016 to 2020, which is close to GAW's compatibility goal for CH_4 (± 2 ppb) (Fig.
35 S1). During the period of GC-FID measurements, the average difference (±1 SD) between KMA and NOAA flasks was 5.2 ± 15.6 ppb, which is greater than the difference since CRDS observations started but reasonable as per the GAW extended compatibility goal of ± 5 ppb.

2.4.2 Regional background selection method

To understand the atmospheric CH_4 measurements and CH_4 growth rate, data representing well-mixed air should be selected for analysis on a regional scale. There are many methods to select data for baseline such as using related tracers, wind speed/direction, or statistical methods (Fang et al., 2015; Chambers et al., 2016; Bacastow et al., 1985; Lowe et al., 1979). For Korea network, we used a statistical method described in detail by Seo et al. (2021).

There are three steps to select the background levels (L3 hourly data) from valid L2 hourly data:

Step 1) $HS(t) \leq A$

Step 2) $|HA(t) - HA(t-1)| \leq B$ or $|HA(t) - HA(t+1)| \leq B$

Step 3) $|HA(t) - 30 \text{ days moving median of HA}| \leq C$.

Where HS represents CH_4 hourly standard deviation, HA is CH_4 hourly means and t represents time in hours. In step 3), t is the middle of the time window. A, B and C are criteria determined empirically for each step, as given in Table 2. C is the standard deviation of 30 days moving average multiplied by α and here $1.8\sigma_{30d}$ is applied to all three stations as C.

Even though the data were selected by step 1) and 2), high CH_4 levels remained because of long-lasting stagnant conditions (e.g. over 6 days). Therefore, we also apply step 3). This process retained 21–52% of the data at each station, which were defined as L3 hourly on observations (Fig. S2). To get L3 daily/monthly data, the method developed by Thoning et al. (1989) was used to fit smooth curves to the daily averages computed by L3 hourly data. The methods reduce noise induced by synoptic-scale atmospheric variability, fill measurement gaps, and are used to represent the regional baseline. The details are described in Appendix B of the supplementary material. Finally, we can get the L3 daily data, L3 monthly data, long-term trend and seasonal amplitude after applying Thoning et al. (1989). The detailed definitions are in Appendix C, supplementary.

Table 2. Criteria and percentage of selected background levels from observed data at each station.

Station ID	AMY	JGS	ULD
Data period	1999 to 2020	2012 to 2020	2012 to 2020
A [ppb]	2.1	2.1	2.8
B [ppb]	4.9	5.2	3.6
C [ppb]	$1.8\sigma_{30d}$ (for all three stations)		
Spring, MAM [%]	29.1	46.6	57.9
Summer, JJA [%]	11.0	33.5	37.6
Autumn, SON [%]	16.9	30.9	53.2
Winter, DJF [%]	28.4	49.1	58.9
Total [%]	21.3	40.64	52.2

CH$_4$ data were produced under the same conditions for all three stations; however, ULD was affected by emissions from a garbage incinerator until Dec. 2016, while AMY was affected by a malfunction of the drying system for 26 Aug-9 Sep. 2016. The garbage incinerator was moved to the northeast part of the island in December 2016. Therefore, we compared data from the three stations from 2016 to 2020, excluding the periods mentioned above.

In section 3.5, for comparison of our station annual/monthly mean and seasonal amplitude to those parameters calculated from other Asian stations, WLG and RYO, we downloaded daily data for these stations from the World Data Centre for Greenhouse Gases (http://gaw.kishou.go.jp). We applied the Thoning et al. (1989) method to each daily data set to get monthly mean and seasonal amplitude to compare. Annual means are averaged by monthly means while annual growths are derived from the difference of consecutive annual means.

2.5   Flask-air data

Long-term data on CH$_4$ and its isotopes (δ^{13}C in CH$_4$, hereafter δ^{13}C$_{(CH4)}$) were collected at TAP, 28 km away from AMY. Samples were collected weekly between 1200 and 1800 (Korea Local Time), when boundary layer height (BLH) was maximum. The collected samples were sent to Boulder, Colorado for measurement of CH$_4$ at NOAA and to INSTAAR (Institute of Arctic and Alpine Research, University of Colorado) for δ^{13}C$_{(CH4)}$ analysis (Miller et al., 2002). Samples were analyzed from 1990 for CH$_4$ and from 2000 for δ^{13}C$_{(CH4)}$. Since TAP and AMY are only 28 km apart, their data are representative of the same region under large synoptic conditions (Fig. S3), especially for well mixed air. These data were thus used to trace the changes in the surrounding environment in East Asia (section 3.5). AMY started flask sampling for CH$_4$ and δ^{13}C$_{(CH4)}$ in December 2013 with same method like TAP and these data were used only for characterization of CH$_4$ at AMY in section 3.4.3.

To understand the regional source signature of excess CH_4 and to consider background atmospheric variations, Miller-Tans plot are used with flask sample data (Miller & Tans, 2003).

$$\delta_{obs}C_{obs} - \delta_{bg}C_{bg} = \delta s(C_{obs} - C_{bg})$$

Here, C and δ refer to CH_4 and $\delta^{13}C_{(CH4)}$, and the subscript bg, obs and s refer to background, observed and source values. Therefore, by plotting $\delta_{obs}C_{obs} - \delta_{bg}C_{bg}$ (y) against $C_{obs} - C_{bg}$ (x), δs indicates the slope of the linear regression represents the source $\delta^{13}C_{(CH4)}$ signature. For background data, we downloaded data of CH_4 and $\delta^{13}C_{(CH4)}$ observed at Mauna Loa (https://gml.noaa.gov/dv/data, last access March 2022).

2.6   Hybrid Single-Particle Lagrangian Integrated Trajectory model (HYSPLIT) cluster analysis

We downloaded and installed the HYSPLIT with window version and used the built-in algorithm. HYSPLIT trajectories were calculated using the Global Data Assimilation and Prediction System (GDAPS) at a horizontal resolution of 25 km to determine the origin of air masses transported to TAP during 2006–2020. The back trajectories were calculated for 96 h periods at 3 h intervals, with 500 m altitude matching the time of each flask-air sample. Based on a cluster analysis, northern China (CN) accounted for 27% of all air masses; these originated in Russia and travelled through Mongolia and northeast China. Southern China (CS) accounted for 6%; these air masses originated from East China sea and the southern part of China. Air masses from Korea local (KL) reflected emissions from the Korean Peninsula and Japan, accounting for 17% of the total air masses. Other sectors were also analyzed, but there were no significant or representative emission signals from Potential Source Strength (section 2.7 below), so they are not reported herein.

2.7   Potential Source Strength (PSS) analysis

To identify and illustrate the potential source distributions for regional pollutions, we calculated the PSS using the trajectory statistics approach, which has often been applied to estimate the potential source areas of greenhouse gases (Reimann et al., 2004, 2008; Li et al., 2017). The trajectory statistics approach was introduced first by Seibert et al. (1994). The underlying assumption of the method is that elevated atmospheric levels at an observation site are proportionally related to the air mass residence time on a specific grid cell over which the observed air mass has been passing. Thus, this method simply calculates the airmass residence time weighted mean abundance (here, units of mole fraction) for target compounds (CH_4 in this study) in the domain with 0.5 × 0.5 grids using the following formula (Eq. 2):

$$\overline{C_{(i,j)}} = \frac{\sum_{a=1}^{M} T_{(i,j,a)} C_a}{\sum_{a=1}^{M} T_{(i,j,a)}} \tag{Eq. 2}$$

where $C_{(i,j)}$ represents the potential source strength of the grid cell i, j as a potential source region of the target compound (CH_4); a is the index of the trajectory; M is the total number of trajectories that passed through cell i, j; C_a is the enhanced mole fraction (difference from background mole fractions described in section 3.2) measured during the arrival of trajectory a; and $T_{(i,j,a)}$ is the

residence time of trajectory a spent over grid cell i, j and which were calculated using the method described by Poirot and Wishinski (1986) as following formula (Eq.3)

$$T_{(i,j,a)} = \sum_{n=1}^{N} \frac{S_{(i,j,n,a)}}{V_{(n,a)}}$$ (Eq. 3)

where $S_{(i,j,n,a)}$ is the length of that portion of the nth segment of a back-trajectory which falls over grid cell i,j. $V_{(n,a)}$ is the average speed of the air parcel as it travels along the nth segment of the a back-trajectory using HYSPLIT model. To ensure trajectory reliability, we used only 4-day (96 h) back-trajectories at an altitude of 500 m above mean sea level. To consider the influence of air masses on emissions at ground level, air masses passing above the boundary layer height (BLH) were excluded. BLH is obtained from the HYSPLIT model. To exclude the influence of emission sources surrounding AMY, enhanced CH_4 data with wind speeds lower than 2 m·s^{-1} were omitted from the PSS analysis. When we compare our PSS results from AMY, JGS, and ULD using CH4xs data from 2016 to 2020, they showed similar source, regions while the coverage and CH4xs are slightly different (Fig. S4.).

3. Results and Discussion

3.1 Measurement uncertainty

Observed CH_4 is influenced by natural atmospheric variability and measurement procedures. Natural atmospheric variability can be represented as the standard deviation of all measurements contributing to a time-average, after accounting for experimental noise. The measurement uncertainty is critical to provide information on data quality so that users can understand the limitations and reliability of measurement. According to previous studies, the total measurement uncertainty consists of multiple uncertainty components (Andrews et al., 2014, Verhulst et al., 2017). For the KMA network, a measurement uncertainty of approximately 0.11 ppm has been calculated for CO_2 with limited but practical components (Lee et al., 2019). Using the same method used for CO_2, we calculated a practical realistic measurement uncertainty for CH_4 in the KMA network (Eq.4). Based on the measurement of target cylinders and a co-located comparison of measurements at AMY and JGS, we assumed systematic biases to be negligible (http://empa.ch/web/s503/wcc-empa, last access: January 2022).

$$(U_T)^2 = (U_{h2o})^2 + (U_P)^2 + (U_r)^2 + (U_{scale})^2$$ (Eq. 4)

where U_T is the total measurement uncertainty in the reported dry-air mole fractions; U_{h2o} is the uncertainty from the drying system; U_p is repeatability; U_r is reproducibility defined as a drift between occurring between calibration episode; and U_{scale} is the uncertainty of propagating the WMO-X2004A CH_4 scale to working standard gases.

U_{h2o} was computed from the differences in H_2O (%) between the ambient airstream through the drying system and standard gases injected directly, bypassing the drying system. An ideal measurement would be through the analysis of the standard gases and air samples after they pass through the same drying system (WMO, 2016). However, our drying efficiency was not constant, so we injected standard gases directly as a reference value of H_2O. Therefore we considered the CH_4 dilution offsets between working standards and sample air while estimating the uncertainty with a similar method using Eq.(1) in section 2.3. Hourly CH_4 dilution maximum offsets are up to 0.009 ppb at AMY, 0.006 ppb at JGS and 0.009 ppb at ULD from 2016 to 2020. This uncertainty term

was smallest (0.006 to 0.008 ppb) among all uncertainty factors in the KMA network as indicating the sampled air has negligible biases through our drying system.

$$U_x = \sqrt{\frac{\sum_{i=1}^{N}(x_i)^2}{N}}$$ (Eq. 5)

where U_x represents U_{h2o}; x is the hourly CH_4 dilution offsets from Eq (1); N is the total number of hourly mean values. U_{h2o} is tabulated for each station in table 3.

We calculated U_r as the standard deviation of all drift using Eq (5), where U_x represents U_r; x_i is the drift occurring between calibration episodes; and N is the total number of data. They are tabulated with other uncertainty terms by site in table 3. We determined U_r as the differences in CH_4 measured from cylinders with subsequent calibrations after two weeks. It ranged from –0.9 to 2 ppb at AMY and from –1.25 to 0.84 ppb at JGS. ULD had a two week calibration periods, which changed to one month from May 18, 2017 to November 11, 2019. During this period of one month calibration frequency, U_r increased to a maximum of 4 ppb, which is greater than the WMO/GAW compatibility goal of ±2 ppb. After conducting the reproducibility test in November 2019, the calibration frequency decreased to 5 days. Therefore, U_r at ULD was separated into two groups including or excluding the period with a longer calibration period (with asterisk in Table 3). When we considered only the period with a higher calibration frequency, the uncertainty at ULD was similar to that at other stations. This means that U_r is the largest component of measurement uncertainty, and that U_T can be decreased using an appropriate calibration strategy.

U_p was determined from the standard deviations of working standard measurements, as described in section 2.3, and expressed by a pooled standard deviation (Eq. 6).

$$U_p = \sqrt{\frac{\sum_{i=1}^{N} N_i \times S_i^2}{N_i - N_t}}$$ (Eq. 6)

where S_i is the standard deviation of 10 min averages of working standard measurements; N_i the index number of a measurement during 10 min (based on 5 s intervals); and N_t is the total number of calibrations during the period. S_i was less than 0.882 ppb at AMY, 0.603 ppb at JGS, and 0.688 ppb at ULD. The pooled standard deviations (U_p) are shown in table 3.

According to Zhao et al. (2006), the uncertainty of working standards can be calculated by the propagation error arising from the uncertainty of primaries with a maximum propagation coefficient ($\gamma = 1$) and repeatability. Similarly, U_{scale} for working standards is determined by (Eq. 7)

$$U_{scale} = \sqrt{U_p^2 + U_{lab}^2}$$ (Eq. 7)

where U_{lab} is the uncertainty of laboratory standards, which CCL (NOAA/GML) certified. Here, U_{lab} has the same value as the uncertainty of secondary standards, 0.3 ppb with a confidence interval of 68%, based on calibration of the secondary standards

against the primary standards (http://gml.noaa.gov/ccl/ch4_scale.html, last access: January 2022). These values were the same for all stations since they were calibrated by a central lab at NIMS in Jeju. Therefore, U_p is the repeatability at the central lab since we propagated the standard scale through the same analyzer and set-up for atmospheric monitoring. This value was always less than 0.12 ppb.

Table 3. Uncertainty estimates for measurements of CH_4 at each station from 2016 to 2020. Units are ppb. All terms are 68% confidence intervals

Uncertainty terms	AMY	JGS	ULD
U_{h2o}	0.006	0.006	0.008
U_p	0.157	0.120	0.351
U_r	0.578	0.365	2.323 (0.710*)
U_{scale}	0.323	0.323	0.323
U_T	0.778	0.728	2.352 (0.801*)

*This value was calculated excluding the period with one-month calibration frequency

For AMY, the difference from the CCL in the RR test with the analysis of the same cylinder was from –0.3 to 1.3 ppb with GC-FID in 2010. Therefore, we considered the largest value of 1.3 ppb as the measurement uncertainty from 1999 to February 2016 during the GC-FID measurement period.

Overall, the total measurement uncertainty was calculated to be from 0.728 to 0.801 ppb. These values were similar to those reported by CRDS measurements (< 1 ppb) (Winderlich et al., 2010; Andrews et al., 2014, Verhulst., 2017). In the future, quoted uncertainties could be greater owing to the inclusion of more error sources, while reproducibility may improve with a different calibration strategy.

3.2 Local/regional effects on observed CH_4

The enhancement of CH_4 relative to the regional background can help evaluate local/regional additions to CH_4, with the excess signal defined as (Eq. 8):

$$CH_{4XS} = CH_{4OBS} - CH_{4BG} \qquad\qquad (Eq. 8)$$

where CH_{4OBS} is L2 hourly data (before filtering) and CH_{4BG} indicates the regional background at a site as determined by the smoothed curve fitted to L3 daily data (section 2.4.2). CH_{4XS} was greatest in the order AMY (55.3±37.7 ppb) > JGS (24.1±10.2 ppb) > ULD (7.4±3.9 ppb) from 2016 to 2020. For ULD, we excluded data collected in 2016 as they were affected by the garbage incinerator next to the station (section 2.4, Figure 2©). All stations showed largest CH_{4XS} in summer (June, July, August) with 109.6 ± 23.8 ppb at AMY, 37.0 ± 2.1 ppb at JGS and 12.2 ± 3.7 ppb at ULD. Conversely, the smallest values were observed as

25.6 ± 2.4 ppb at AMY and 18.8 ± 4.1 ppb at JGS in spring (March, April, May), while the lowest value of 7.5 ± 0.4 ppb at ULD was observed in winter (December, January, February). The baseline selection conditions listed in Table 2 also supported this result. The selected baseline data accounted for only 11–37.6% of summer data at all stations, indicating that CH_4 levels were elevated in summer. In winter and spring, we could better capture well mixed air compared with other seasons (28.4–58.9%) because of the strong westerly wind with Siberian high.
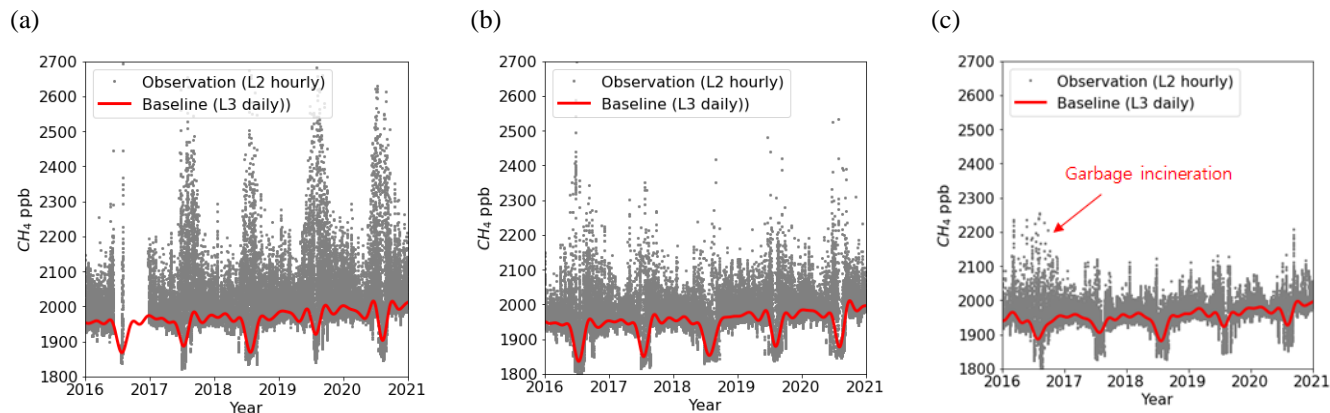
Figure 2. L2 hourly (grey scatters, observation) and fitted L3 daily data (red line, Baseline) at (a) AMY, (b) JGS, and (c) ULD from 2016 to 2020.

To understand the influence of local surface wind on observed CH_4, bivariate polar plots were used for 2018, the year least-affected by typhoons compared to other years.

These plots express the dependence of all hourly CH_4 (L2 hourly data before selecting baseline) on wind direction and speed (Fig. 3–5). The wind data were derived from an AWS, as described in section 2.1.

At AMY, when wind speed was consistently < 3 m·s⁻¹, CH_4 was elevated during all seasons. Especially in summer, it showed strong signals when wind direction was between 45° and 135° (from land). A similar observation was made in other seasons, possibly indicating that this was related to local influences such as from rice paddies. The dominant wind direction was south-west in summer and north-west in winter. Even though lower CH_4 levels were captured regardless of wind direction with increased wind speed, CH_4xs was still higher than that at the other two stations. Therefore, AMY could be affected not only by local activities but also by distant emissions.

JGS experienced the strongest winds among the three stations in all seasons (maximum 27.5 m·s⁻¹). Strong north-westerly wind (open sea) occurred in spring and winter, and air masses from the north-east (Korean inland) were noted during autumn and from the south (open sea) during summer. CH_4 was lower than at AMY, with strong signals observed in all seasons under different criteria. Higher CH_4 levels occurred because of winds from the eastern part of JGS in autumn and summer when the wind speed decreased to less than 5 m·s⁻¹. For spring and winter, strong signals were noted in the eastern and northern parts of JGS. Since JGS is located downwind from continental Asia and strong westerly winds occur in winter/spring because of the strong Siberian high, this signal might be related to activities not only in Asia but also in Jeju.

For ULD, the main wind directions were quite clearly from 0° to 90° (30%) and from 180° to 270° (33%), and wind speeds less than 5 m·s⁻¹ occurred 72% of the total time. High CH_4 episodes were mainly observed when the wind direction was between 180°

and 225°, presumably affected by the southeastern part of the Korean Peninsula. This wind direction was very dominant in summer with a lower wind speed than that in other seasons.

Overall, atmospheric CH₄ observed by KMA GAW stations was affected not only by the local area but also by air masses from continental Asia, as indicated by the results from synoptic systems. Signals at AMY may be affected by local/regional activities, such as agriculture and livestock industries, owing to the relatively lower wind speeds; however, it still showed higher values compared with those of other stations when it captured well-mixed air. This indicates that AMY was affected not only by local sources but also by long range transport of air masses originating from continental Asia. ULD showed lower CH₄ and was less affected by local impacts.
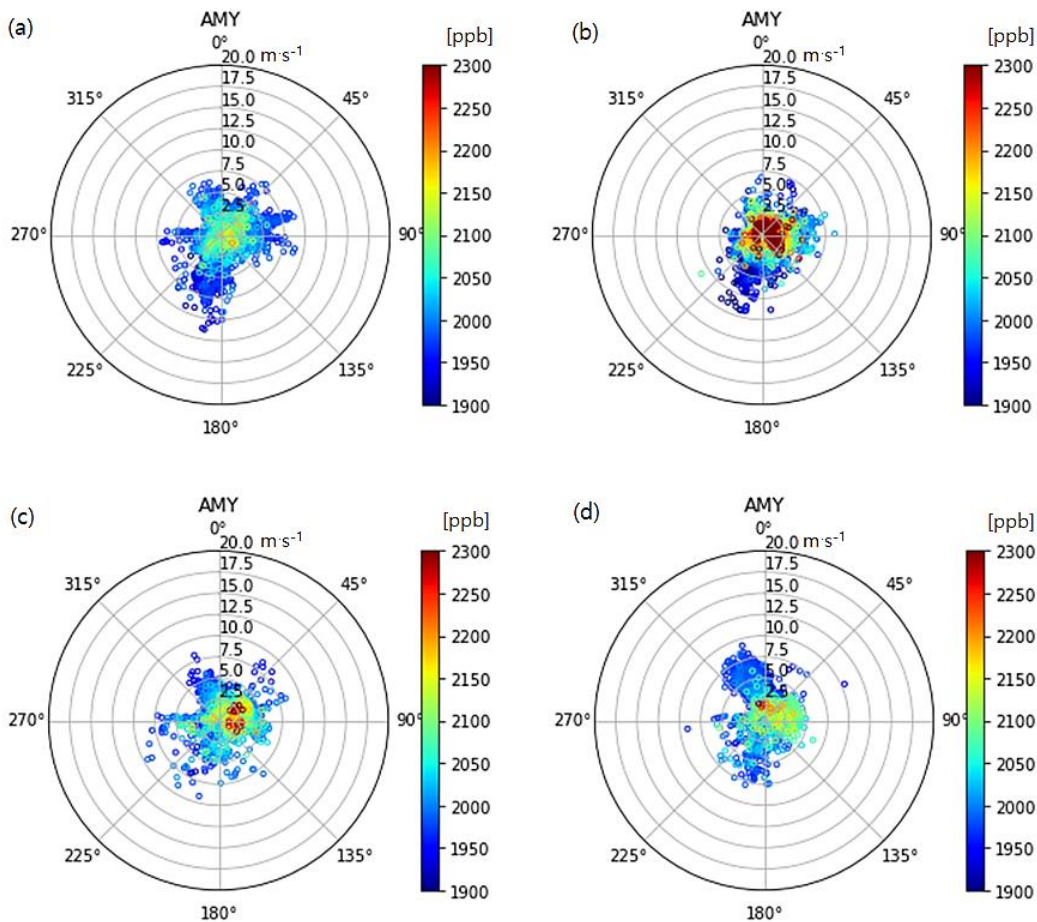
Figure 3. Bivariate polar plots for observed CH₄ (L2 hourly) in spring (a), summer (b), autumn (c), and winter (d) at AMY in 2018.
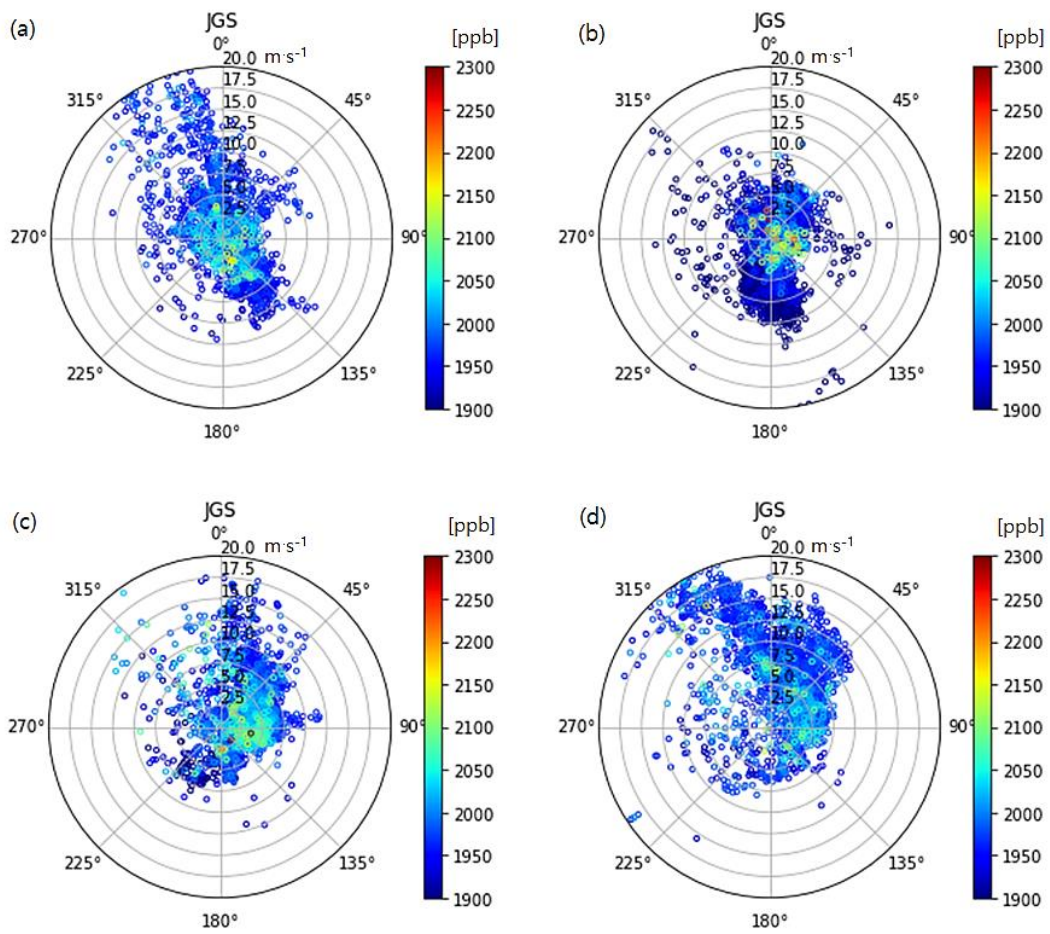
Figure 4. Bivariate polar plots for observed CH$_4$ (L2 hourly) in spring (a), summer (b), autumn (c), and winter (d) at JGS in 2018.
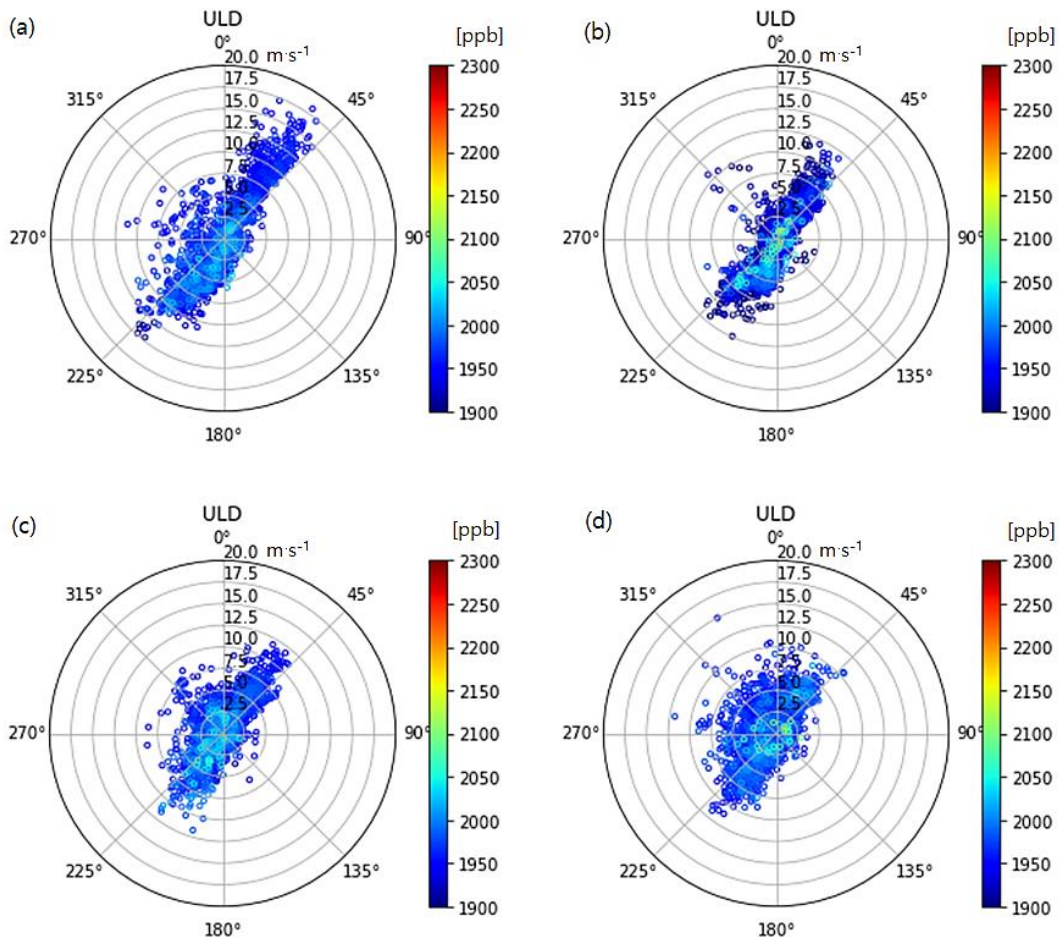
Figure 5. Bivariate polar plots for observed CH$_4$ (L2 hourly) in spring (a), summer (b), autumn (c), and winter (d) at ULD in 2018.

3.3   Average diurnal variation

Diurnal CH$_4$ variations were calculated as the average deviation from the daily mean in each month from L2 hourly data from 2016 to 2020 (recent 5 years) for AMY and JGS, and from 2017 to 2020 for ULD (Fig. 6).

Among the three stations, the mean diurnal variation of all seasons was greatest at AMY (69.5±49 ppb) and smallest at ULD (7.6±4.2 ppb), while it was 24.7±14.4 ppb at JGS. Daily variations in CH$_4$ are generally small at global scale stations, so stations with a large seasonal cycle amplitude may be affected by local/regional sources (Aoki et al., 1992) and transport driven such as upslope/downslope air and land/see breeze due to geographical reason.

AMY was surrounded by CH$_4$ sources as described in the introduction, while ULD had similar characteristics to global scale stations that are less impacted by their local/regional environment. Similar to ULD, Mt. Waliguan station (3816 m), a representative global GAW station in Asia, also showed an amplitude of 5 to 10 ppb for the diurnal CH$_4$ cycle (Zhou et al. 2004., Fang et al., 2013).

Atmospheric CH$_4$ at AMY and JGS started to increase around midnight and peaked from 5 to 8 AM local time and then decreased with minimum value from 1500 to 1800. For ULD, the peaks were observed between 6 to 11 AM, especially in summer, but there were no significant troughs. These variations at AMY and JGS were consistent with the changes in wind pattern and BLH. BLH

was maximum near the middle of the day. At night, cooling caused by radiation loss at ground level leads to a stable boundary layer, leading to accumulation of CH_4 (Worthy et al., 1998, Higuchi et al., 2003). Both stations were also affected by land-see-breeze and received air from seaside during the daytime, which enhanced the diurnal variation. These patterns of CH_4 were similar to those of CO_2 observed by both stations (Lee et al., 2019) because of similar meteorological conditions. However, ULD is located on the slope of a mountain and is surrounded by complex terrain, thus being affected by certain winds from north to east and south to west, regardless of time and season. However, peak values only occurred during 6 to 11 AM, which needs further study.

All stations showed the lowest amplitude in winter (Dec. to Feb.) and the largest amplitude in summer (Jun to Aug.). AMY showed the largest diurnal amplitude (176.8±74.6 ppb) in August among the three stations, which was almost 2.5 times greater than the annual mean value, with substantial variation among months. JGS and ULD showed the largest amplitude in August (43.4±17.7 ppb) and July (17.2±11.6 ppb), respectively. This indicated that the emission and meteorological impacts (e.g. maximized BLH and land-see breeze) were strong in summer. AMY is close to rice paddies (110 km^2), which are the major source of CH_4 in summer. JGS and ULD are not close to waterlogged paddies. However, high temperatures stimulate greater emissions from sources such as agriculture, livestock, and wetlands, thus affecting emissions at both stations. Similar to the observation made at AMY, previous studies have shown large variation in CH_4 emissions from the rice paddy area (196±65 ppb) and wetland (~150 ppb) during summer (Worthy et al. 1998., Fang et al., 2013).

(a)

(b)

(c)
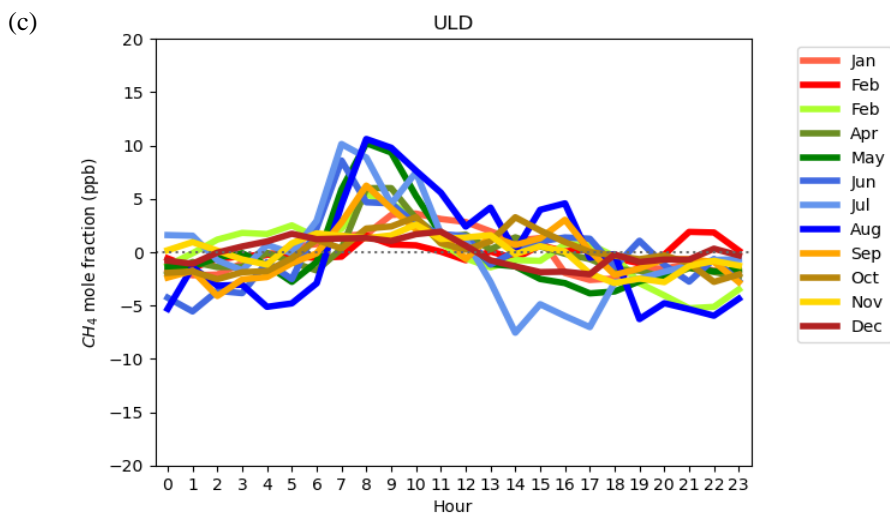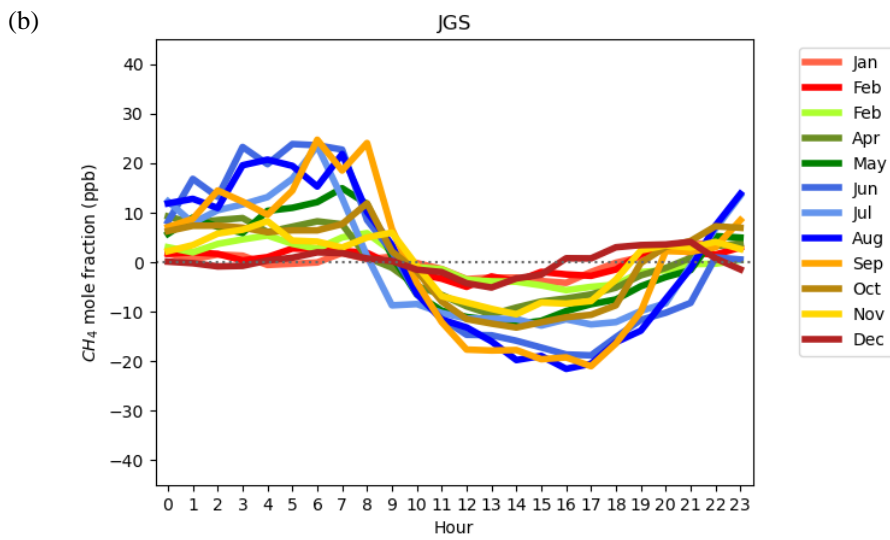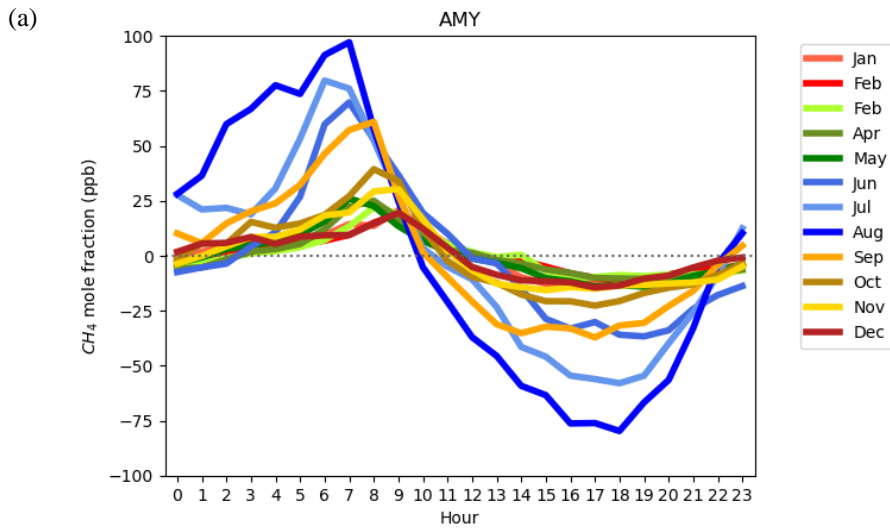
Figure 6. Mean diurnal variations of CH$_4$. Values show the average departure from the daily mean in each month at (a) AMY and (b) JGS from 2016 to 2020 and (c) at ULD from 2017 to 2020.

3.4   Comparison with other East Asian stations: annual mean, seasonal amplitude, and growth rate

3.4.1 Annual mean

Time series of monthly mean CH$_4$ from KMA's three stations and the two other stations in East Asia are compared in Fig. 7(a) and annual mean CH$_4$ is summarized in Table 4. Annual CH$_4$ mean was the highest at AMY and the lowest at WLG. The other stations showed similar levels of annual mean considering standard deviations. It was obvious that AMY was affected by local and regional activities, while WLG was affected by representative air masses of the Northern Hemisphere.

3.4.2 Seasonal amplitude

As described in section 2.4, the seasonal amplitudes of CH$_4$ from 2016-2020 was calculated for three KMA stations and are compared with those values from WLG and RYO (Table 4). The seasonal amplitude is related to the seasonal atmospheric transport, for example major wind direction, the combination of CH$_4$ surface flux distribution and chemical loss by reactions with OH and by soil loss. Seasonal amplitudes followed the order JGS > AMY > ULD>RYO> WLG (Table 4).

Since WLG is a global baseline station that is affected less by regional sources and sinks, the amplitude was smallest compared with the other regional stations. The amplitude of WLG was similar to that of other global stations such as Mauna Loa (30.6±4.2 ppb) (Dlugokencky et al., 1995). Seasonal amplitudes at AMY and JGS are much greater than at the other 3 stations, and even inland regional stations in China, such as Lin'an (77±35 ppb) and Longfenshan (73±8 ppb) (Fang et al., 2013). Minimum values at JGS are -14.8±9.2 ppb lower than AMY minimum values while the maximum values at both stations are similar. Li et al. (2018) reported that summer airmass were affected by large-scale low-level monsoonal circulation across the tropic in Jeju. A similar meteorological impact for CH$_4$ was reported at TAP (Dlugokencky et al., 1993). Even though transport and OH radical can result in low CH$_4$ values at AMY, the station is also affected by nearby sources with enhanced emissions during summer. As we introduced in section 2.1, AMY has large rice paddies and livestock industries within 50 km. During summer, high temperatures will enhance CH$_4$ emissions from these sources, leading to higher CH$_4$ than that at JGS (Kenea et al., 2021; Wang et al., 2021). Among regional stations, ULD and RYO may be less affected by regional flux because of their altitude, causing their amplitude to be greater than that of WLG but smaller than that of AMY or JGS.

Minimum values were observed in summer, while maximum values occurred in spring, autumn, or winter for different regional stations. In contrast, WLG showed maximum levels in summer and minimum values in winter/spring. Zhang et al. (2013) reported that regional/local sources and air masses from polluted regions influenced by industry, crop residue burning, and agriculture may affect CH$_4$ observations at WLG in summer.
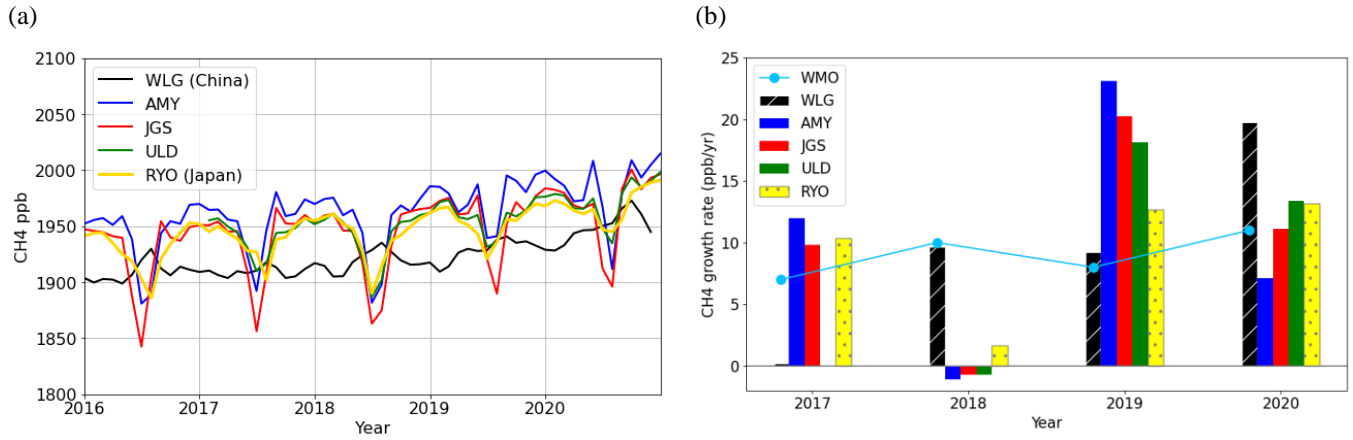
Figure 7. Time series of (a) monthly mean CH_4 and (b) annual growth rate at WLG, AMY, JGS, ULD, and RYO. The growth rate reported by WMO (WMO, 2021) is overlaid on (b) and this value is calculated as the change in annual mean from the previous year.

Table 4. Annual mean CH_4 with standard deviations from monthly mean from 2016 to 2020, mean seasonal amplitudes, and growth rates. Seasonal cycle amplitude during each calendar year was magnitude of the peak to trough of the detrended seasonal cycle (see section 2.4.2). The growth rate is an annual increase (not de-seasonal), absolute difference from previous year. Growth rate at ULD was calculated only from 2017 to 2020. Units are dry-air mole fractions (ppb)

Year	WLG	AMY	JGS	ULD	RYO
2016	1909±9	1942±28	1928±33	-	1929±19
2017	1909±4	1954±24	1938±31	1942±15	1939±15
2018	1919±9	1953±31	1937±35	1941±24	1941±21
2019	1928±10	1976±19	1957±26	1959±13	1954±14
2020	1948±14	1983±27	1968±32	1972±17	1967±14
Mean seasonal amplitude over 5 years.	21±5	100±13	118±9	67±12	58±8
Mean annual growth rate over 5 years (ppb·yr^{-1})	10±8	10±10	10±9	10±10	10±5

3.4.3 Growth rate

The annual increasing/decreasing was calculated the difference in annual means from the previous year (Fig.7 (b)). When we analyzed the overall growth rate for 5 stations, mean values of annual growth rate from 2017 to 2020 were around 10 ppb·yr^{-1}, which was similar to the WMO global mean (9±2 ppb·yr^{-1}). However, when yearly comparisons were made, WLG and the other

4 regional stations varied. Especially from 2016 to 2017, WLG showed no increase in CH₄, while CH₄ at other stations showed small or negative increases from 2017 to 2018. Normally the growth rate in CH₄ at WLG matches well with the WMO global increase/decrease trend (Fig. 7. (b)). Wang et al.(2021) reported that CH₄ fluxes in Asia are influenced by ENSO and temperature; therefore, we compared the growth rate of CH₄ from four regional stations with both factors (Fig. S5). This showed that the pattern

5   of growth rate was quite similar to that of ENSO; however, even though the ENSO was negative (e.g., from 2017 to 2018) when surface temperature was high, the growth rate still increased. Miller-Tans plots shows the signature of CH₄ increments into background air of Mauna Loa (Fig. S6). And the slope was –52.3±2.2‰ in winter and –53.7±0.7‰ in summer at AMY during 2016 to 2020. These values are very similar to the observed values during the summer vegetation period when biogenic emissions are very active (–52.5±1.9‰) in Europe (Varga et al., 2021), indicating that AMY was mainly affected by biogenic sources

10   regardless of the season during this period. Throughout Asia, emissions from agriculture and waste account for over 50% of the total, which is increasing every year (Jackson et al., 2020). Since climate variability such as ENSO and temperature drive biogenic sources, the CH₄ growth rates observed at regional stations in Asia are more sensitive to regional emissions than the global station.

3.5   Long-term records of CH₄ and its drivers in East Asia
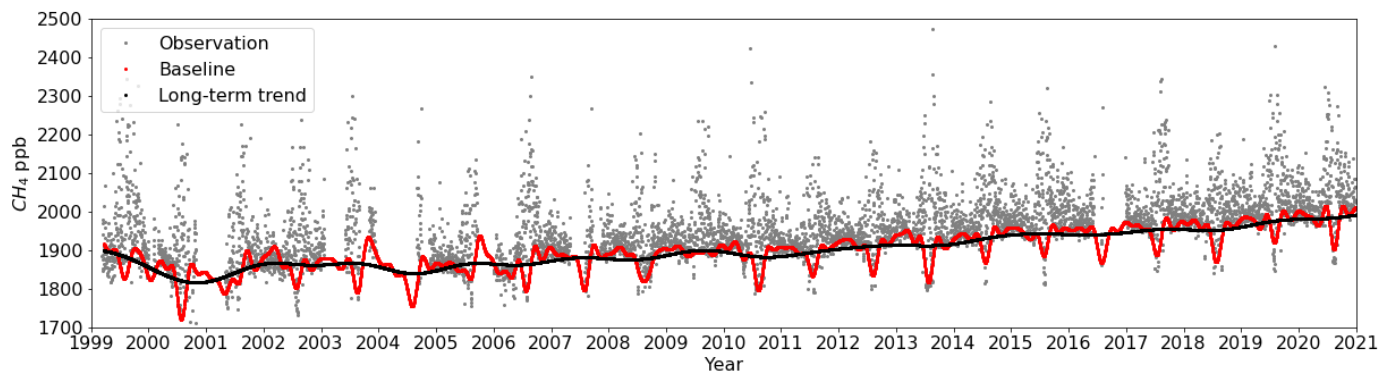
Figure 8. Time series of CH₄ (L2 daily, grey), baseline (L3 daily, red), and long-term trend (black) observed at AMY from 1999 to 2020.

20   In Figure 8, the black line is the long-term CH₄ trend after seasonal cycle has been removed (Appendix C in supplementary). In 2009 there is no clear seasonal cycle because there was an instrumental malfunction in summer. The long-term trend at AMY was very similar to the global trend. From 1999 to 2005, the mean annual CH₄ growth rate (absolute differences from the previous year) was approximately –1.2 ppb·yr⁻¹ at AMY, while the global value was 0.3 ppb·yr⁻¹ and both values have increased since 2006. CH₄ increased by 3.3 ppb·yr⁻¹ from 2006 to 2010 (global: 5.9 ppb·yr⁻¹) and by 8.3 ppb·yr⁻¹ (global : 9 ppb·yr⁻¹) from 2016 to 2020,

25   indicating that the growth rate is accelerating.

To understand the source regions affected AMY CH₄ level, we analysed PSS with hourly CH₄xs from 2006 to 2020. CH₄xs did not vary much and was 49±74 ppb during 2006–2010 and 50±70 ppb during 2016–2020. According to the PSS analysis, affecting major source regions were CN, CS and KL sectors (Fig. 9 (a)). Sources affecting CS and KL are paddy and livestock fields and that for CN was reported to be fossil fuel emissions mainly (Zhang et al., 2011, Ito et al., 2022, Chen et al., 2022).

Through the HYSPLIT cluster analysis from 2006 to 2020, we categorized the TAP $\delta^{13}C_{(CH4)}$ data and selected the samples only affected by each source regions, CN, CS, and KL, respectively (section 2.6). Using TAP $\delta^{13}C_{(CH4)}$ long-term data from 2006 to 2020 affected by CN, CS and KL, Miller-Tans plots indicated that emissions from CN were mainly related to fossil fuel or biomass burning (–44.3±1.8‰), while CS (–56.1±1.5‰) and KL (– 54.6±1.2‰) were affected more by biogenic sources during 2006–

5   2020 (Fig.9 (b)). Sherwood et al. (2017) reported unweighted global mean $\delta^{13}C$ of -44.8±10.7‰ from fossil fuel use, -26.2±4‰ from biomass burning, and –61.7±6.2‰ from microbial sources. Regionally CH_4 emissions from wetlands in Siberia are at -69.9±5.5‰ while in Hong Kong it was more enriched at -56.9±3.8‰ (Ganesan et al.,2018). In northern China, a high coal emission area, heavy CH_4 signal appears from -35‰ to -50‰ (Feinberg et al., 2018). Even though the uncertainty of isotopic source signature is quite large, CH_4 formed at high temperature such as combustion is enriched in the heavier isotope while CH_4

10   from wetland, rice paddies and livestock is depleted. Therefore, our isotope analysis was well matched to reported source regions. On the other hand, isotope signatures were shifted slightly in China (CN and CS) while for Korea (KL) it was steady in the uncertainty range from 2006 to 2020. When we analyze the Miller-Tans plots in every 5 years (Fig. S7), for CN the slope was -38±3‰ in 2006/10 but it became depleted -45±2.4‰ in 2016/20 while those value was enriched from -59.8±1.5‰ to -51.9±2.5‰ in CS. KL showed the quite constant values from -55±1.6 to -54±3.1‰ in the same period. This suggested that

15   CH_4 growth rate in East Asia was affected by not only biogenic but also pyrogenic sources such as biomass burning and fossil fuel. The recent global accelerated increase in atmospheric CH_4 was more related to microbial sources such as agriculture and wetland (Lan et al., 2021, Basu et al., 2022).

Since the CH_4 emissions from agriculture and livestock accounted for 30% and 36% in China and Korea respectively in 2020 (Crippa et al., 2022), CH_4 might be increased by temperature impacts on biogenic CH_4 sources. However, fast urbanization and

20   increased energy consumption also can affect these regions. Especially the coal emissions decreased from 2010 in China (Liu et al., 2021) but the coal to gas policy led to increase natural gas consumptions in China (Wang et al., 2022).

Overall, AMY and global growth rates were renewed in 2006 and accelerated during 2006–2020; the increasing trend could be linked to mixed biogenic and fossil fuel sources in East Asia while global to more biogenic sources.
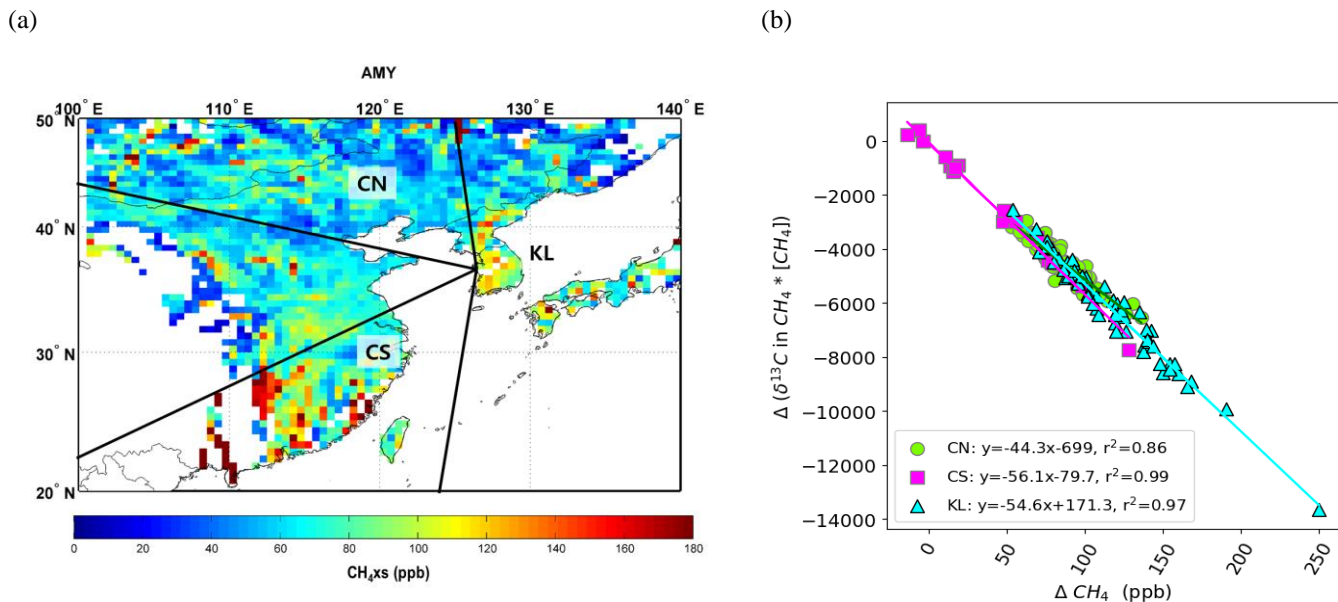
Figure 9. (a) PSS analysis with CH₄xs observed at AMY and (b) "Miller-Tans" plots from 2006 to 2020. Miller-Tans plots showing the source signature of methane increments (TAP) into background air (Mauna-Loa).

4.   Summary and Conclusions

Among greenhouse gases, CH₄ emission reductions can be highly effective for short-term global warming mitigation because of its relatively short lifetime. However, its sources are diverse and yet to be evaluated completely through high accuracy measurements. Our study analyzed CH₄ characteristics observed at regional KMA GAW stations, uncertainties related to its measurement, and changes in sources using long-term data in South Korea.

KMA started monitoring atmospheric CH₄ in 1999 at AMY and expanded its network to the south and east parts of Korea at JGS and ULD in 2012 using a new system consisting of CRDS and a cryogenic drying system.

All three stations have similar measurement uncertainty from 2016 to 2020, in the range of 0.73–0.80 ppb. These uncertainties are similar to values reported in previous studies (less than 1 ppb). In addition, we confirmed reproducibility as the greatest contributor to measurement uncertainty; therefore, calibration strategies are the most critical component for reducing measurement uncertainty.

CH₄xs assessed relative to local background levels at each station was in the order AMY (55.3±37.7 ppb) > JGS (24.1±10.2 ppb) > ULD (7.4±3.9 ppb). CH₄xs was greatest in summer and lowest in spring or winter. This result is consistent with wind direction and speed. In summer, local biogenic sources affected observed CH₄. Low wind speed enhanced CH₄xs, while lower CH₄ levels were observed when the stations experienced high wind speed. For AMY, even when CH₄ was measured in well-mixed air, its level was higher than that at other stations, indicating that it was affected not only by local sources but also by distant air masses from Asia. ULD showed representative CH₄ levels without local impacts. Diurnal variations were greatest at AMY and smallest at ULD, and were affected by local sources and meteorological characteristics. The variation at ULD was 7.6±4.2 ppb, similar to

that at the WLG baseline station in China (5 to 10 ppb). All stations had large diurnal cycles in summer, indicating a strong influence of local biogenic sources at KMA sites.

When CH_4 seasonal cycle amplitudes measured at KMA stations were compared with those at other East Asian stations from 2016 to 2020, the following descending order was observed: JGS (103 ± 10) > AMY (85 ± 16) > ULD (58 ± 12) and RYO (57 ± 12) > WLG (30 ± 11). As discussed, since AMY reflected strong local influences not only in winter but also in summer, its seasonal amplitude was smaller than that of JGS. However, annual CH_4 mean was highest at AMY and lowest at WLG. The relative contributions of CH_4 source types to signals at regional stations in Asia are sensitive to temperature and ENSO. Based on analysis of $\delta^{13}C_{(CH4)}$ measurements, we established an increase in CH_4 from biogenic sources.

From the long-term analysis of CH_4 data at AMY, average CH_4 growth rate was 3.3 ppb·yr^{-1} during 2006–2010, but increased to 8.3 ppb·yr^{-1} in 2016–2020 as similar to the global trend. Through the source distributions determined with our PSS analysis using CH_4xs data, CN, CS and KL sectors were main regions to affect atmospheric CH_4 observed at AMY. Isotope signature based on Miller-Tans plots at CN represents fossil fuel or burning activities while CS and KL biogenic sources during 2006-2020. However, we infer atmospheric CH_4 drivers changes in air masses arriving from China sector, CN and CS. For East Asia the increasing trend could be linked to mixed biogenic and fossil fuel sources while globally the increase was dominate by microbial sources (e.g. agriculture and wetland). Through this study, we confirmed that long-term high-quality data can help understand changes in CH_4 emissions in East Asia. Also, further studies are necessary based on observations to understand sources changes in East Asia since there is a discrepancy between reported inventory and observations (Wang et al., 2022).

Data availability
Atmospheric CH_4 data in KMA network can be downloaded from World Data Centre for Greenhouse Gases (https://gaw.kishou.go.jp) and Korea climate portal (http://climate.go.kr/home/09_monitoring/search/search). TAP CH_4 and $\delta^{13}C_{(CH4)}$ data can be downloaded from ftp://aftp.cmdl.noaa.gov/data/trace_gases/. RYO and WLG data are downloaded from World Data Centre for Greenhouse Gases.

Author contributions
HL designed the study, analyzed the data and wrote the manuscript. WS implemented the data QA/QC. SL implemented PSS analysis. SL run the central calibration centre for KMA stations and provide the calibration strategy. WS, SL, SL, SK and SJ reviewed the manuscript. All authors contributed this work.

Acknowledgments.
We appreciate all staff and technicians at AMY, JGS, ULD in the Korea meteorological network, WLG in China and RYO in Japan. Also special thanks to Dr. Ed Dlugokencky at NOAA and Dr. Sylvia Michel at Colorado University for the support of this study. This work was funded by the Korea Meteorological Administration Research and Development Program "Development of Integrated Climate Change Monitoring and Analysis Techniques" under Grant (KMA2018-00324).

References

Aoki, S., T. Nakazawa, S. Murayama, and S. Kawaguchi, Measurement of atmospheric methane at the Japanese Antarctic Station, Syowa, Tellus, Ser. B, 44, 273–281, doi:10.1034/J.1600-0889.1992.t01-3-00005. 1992

Andrews, A. E., J. D. Kofler, M. E. Trudeau, J. C. Williams, D. H. Neff, K. A. Masarie, D. Y. Chao, D. R. Kitzis, P. C. Novelli, C. L. Zhao, E. J. Dlugokencky, P. M. Lang, M. J. Crotwell, M. L. Fischer, M. J. Parker, J. T. Lee, D. D. Baumann, A. R. Desai, C. O. Stanier, S. F. J. De Wekker, D. E. Wolfe, J. W. Munger, P. P. Tans: CO_2, CO, and CH_4 measurements from tall towers in the NOAA Earth System Research Laboratory's Global Greenhouse Gas Reference Network: instrumentation, uncertainty analysis, and recommendations for future high-accuracy greenhouse gas monitoring efforts, Atmos. Meas. Tech., 7, 647-687, 2014

Bacastow, R. B., C. D. Keeling, and T. P. Whorf, Seasonal amplitude increase in atmospheric CO2 concentration at Mauna Loa, Hawaii, 1959~1982. J. Geophys. Res. Atmos., 90, 10529-10540, doi:10.1029/JD090iD06p10529. 1985

Basu, S. X. Lan, E. Dlugokecnky, S. Michel, S. Schwietzke, J. B. Millar, L. Bruhwiler, Y. Oh, P. P. Tans, F. Apadula, L. V. Gatti, A. Jordan, J. Necki, M. Sasakawa, S. Morimoto, T. Di Iorio, H. Lee, J. Arduini, and G. Manca: Estimating emissions of methane consistent with atmospheric measurements of methane and $\delta^{13}C$ of methane. Atmos. Chem. Phys. 22, 23, 15351-15377. doi.org/10.5194/acp-22-15351-2022, 2022

Chambers, S. D., and Coauthors, Towards a universal "Baseline" characterisation of air masses for high and low-altitude observing stations using radon-222. Aerosol Air Qual. Res., 16, 885-899, doi:10.4209/aaqr.2015.06.0391, 2016

Crippa, M., D. Guizzardi, M. Banja, E. Solazzo, M. Muntean, E. Schaaf, F. Pagani, F. Monforti-Ferrario, J. Olivier, R. Quadrelli, A. Risquez Martin, P. Taghavi-Moharamli, G. Grassi, S. Rossi, D. Jacome Felix Oom, A. Branco, J. San-Miguel-Ayanz and E. Vignati.: CO_2 emissions of all world countries - 2022 Report, EUR 31182 EN, Publications Office of the European Union, Luxembourg, doi:10.2760/730164, JRC130363, 2022

Dlugokencky E. J., Harris J. M., Chung Y. S., Tans P. P., Fung I., The relationship between the methane seasonal cycle and regional sources and sinks at Tae-ahn Peninsula, Korea. Atmos. Environ. 27A:2115–2120. 1993

Dlugokencky, E. J., L. P. Steele, P. M. Lang and K. A. Masarie, Atmospheric CH4 at Mauna Loa and Barrow Observatories: presentation and analysis of in in situ measurements, J. Geophys. Res., 100(D11), 23103–23113, doi:10.1029/95jd02460, 1995

Fang, S.-X., L.-X. Zhou, K. A. Masarie, L. Xu, and C. W. Rella, Study of atmospheric CH_4 mole fractions at three WMO/GAW stations in China, JOURNAL OF GEOPHYSICAL RESEARCH: ATMOSPHERES, 118, 4874–4886, 2013

Fang, S. X., P. P. Tans, M. Steinbacher, L. X. Zhou, and T. Luan, Comparison of the regional CO2 mole fraction filtering approaches at a WMO/GAW regional station in China. Atmos. Meas. Tech., 8, 5301-5313, doi:10.5194/amt-8-5301-2015, 2015

Feinberg, A. I., Coulon, A., Stenke, A., Schwietzke, S., & Peter, T.: Isotopic source signatures: Impact of regional variability on the δ13CH4 trend and spatial distribution. Atmospheric Environment, 174, 99–111. https://doi.org/10.1016/j.atmosenv.2017.11.037, 2018

Ganesan, A. L., A. C. Stell, N. Gedney, E. Comyn-Platt, G. Hayman, M. Rigby, B. Poulter, and E. R. C. Hornibrook: Spatially Resolved Isotopic Source Signatures of Wetland Methane Emissions. Geophys. Res. Lett., 45,3737-3745, https://doi.org/10.1002/ 2018GL077536, 2018.

Graven, H.D., Guilderson, T.P., and Keeling, R.F.: Observations of radiocarbon in CO_2 at La Jolla, California, USA 1992-2007: Analysis of the long-term trend, J.Geophys.Res.,117,D02302, https://doi.org/10.1029/2011JD016533, 2012

Higuchi, K., Worthy, D., Chan, D., and Shashkov, A.: Regional source/sink impact on the diurnal, seasonal and inter-annual variations in atmospheric CO2 at a boreal forest site in Canada, Tellus B, 55, 115–125, 2003.

IPCC, 2021: Summary for Policymakers. In: Climate Change 2021: The Physical Science Basis. Contribution of Working Group I to the Sixth Assessment Report of the Intergovernmental Panel on Climate Change [Masson-Delmotte, V., P. Zhai, A. Pirani, S. L. Connors, C. Péan, S. Berger, N. Caud, Y. Chen, L. Goldfarb, M. I. Gomis, M. Huang, K. Leitzell, E. Lonnoy, J.B.R. Matthews, T. K. Maycock, T. Waterfield, O. Yelekçi, R. Yu and B. Zhou (eds.)]. Cambridge University Press. In Press

Ito, A., S. Inoue and M. Inatomi, Model-based evaluation of methane emissions from paddy fields in East Asia, Journal of Agricultural Meteorology 78(2), 56-65, 2022

Jackson, R. B., M. Saunois, P. Bousquet, J. G. Canadell, B. Poulter, A. R. Stavert, P. Bergamaschi, Y. Niwa, A. Segers and A. Tsuruta, Increasing anthropogenic methane emissions arise equally from agricultural and fossil fuel sources, Environ. Res. Lett. 15, https://doi.org/10.1088/1748-9326/ab9ed2, 2020

Janssens-Maenhout, G.; M. Crippa, D. Guizzardi, M. Muntean, E. Schaaf, F. Dentener, P. Bergamaschi, V. Pagliari, J. G. J. Olivier, J. A. H. W. Peters, J. A. van Aardenne, S. Monni, U. Doering, A. M. R. Petrescu, E. Solazzo, G. D. Oreggioni: EDGAR v4.3.2 Global Atlas of the three major greenhouse gas emissions for the period 1970–2012, Earth Syst. Sci. Data, 11, 959–1002, https://doi.org/10.5194/essd-11-959-2019, 2019

Kai, F. M., S. C. Tyler, J. T. Randerson, and D. R. Blake (2011), Reduced methane growth rate explained by decreased Northern Hemisphere microbial sources, Nature, 476(7359), 194– 197., 2011

Kim, H.-S., Yong S. Chung, P. P. Tans, Dlugokencky, E. J., Decadal trends of atmospheric methane in East Asia from 1991 to 2013, Air Qual Atmos Health, 8. 293-298, 2015

Kenea, S. T., H. Lee, S. Joo, S. Li, L. D. Labzovskii, C.-Y. Chung, Y.-H. Kim, Interannual Variability of Atmospheric CH4 and Its Driver Over South Korea Captured by Integrated Data in 2019, Remote Sens. 2021, 13, 2266. https://doi.org/10.3390/rs13122266, 2021

Lan, X., E. G. Nisbet, E. J. Dlugokencky and S. E. Michel, What do we know about the global methane budget? Results from four decades of atmospheric CH4 observations and the way forward, Philos. Trans. R. Soc. A., https://doi.org/10.1098/rsta.2020.0440, 2021

Lee, H., Han, S.-O., Ryoo, S.-B., Lee, J.-S., and Lee, G.- W.: The measurement of atmospheric CO2 at KMA GAW regional stations, its characteristics, and comparisons with other East Asian sites, Atmos. Chem. Phys., 19, 2149–2163, https://doi.org/10.5194/acp-19-2149-2019, 2019.

Lee, S., H. Lee, S. Kim, Y.-H., Kim, Inter-comparison Experiment for Korea GAW Network to Improve the GHGs Measurement Quality, Journal of Korean Society for Atmospheric Environment, 37, 5, 790-802, 2021

Li, S., S. Park, J.-Y. Lee, K.-J. Ha, M.-K. Park, C. O. Jo, H. Oh, J. Mühle, K.-R. Kim, S. A. Montzka, S. O'Doherty, P. B. Krummel, E. Atlas, B. R. Miller, F. Moore, R. F. Weiss, S. C. Wofsy.: Chemical evidence of interhemispheric air mass intrusion into the Northern Hemisphere mid-latitudes, Scientific Report, DOI:10.1038/s41598-018-22266-0, 2018

Li, S., Y. Kim, J. Kim, S.T. Kenea, T.-Y. Goo, L.D. Labzovskii, and Y.H. Byun.: In Situ Aircraft Measurements of CO_2 and CH_4: Mapping Spatio-Temporal Variations over Western Korea in High-Resolutions, Remote Sens., 12(18), 3093, https://doi.org/10.3390/rs12183093, 2020

Li, S., H. Lee, M.-K. Park, C.-Y. Chung, Y.-H. Kim.: Analysis of CH_4 Source Distributions Based on CH_4-C_2H_6-CO Correlation from KMA Aircraft Regular Observation in 2019 and KORUS-AQ Campaign in 2016 over South Korea, J. Korean Soc. Atmos. Environ. 38(1), 74-87, https://doi.org/10.5572/KOSAE.2022.38.1.74, 2022

Li, S., M.-K., Park, J.-C., Ok, S. Park.: Emission estimates of methyl chloride from industrial sources in China based on high frequency atmospheric observations, J. Atmos. Chem., 74, 2, 227-243, 10.1007/s10874-016-9354-4, 2017

Liu, G., S. Peng, X. Lin, P. Ciais, X. Li, Y. Xi, Z. Lu, J. Chang, M. Saunois, Y. Wu, P. Patra, N. Chandra, H. Zeng, and S. Piao, Recent Slowdown of Anthropogenic Methane Emissions in China Driven by Stabilized Coal Production, Environ. Sci. Technol. Lett. 8, 739−746, https://doi.org/10.1021/acs.estlett.1c00463, 2021

Lowe, D. C., P. R. Guenther, and C. D. Keeling, The concentration of atmospheric carbon dioxide at Baring Head, New Zealand. Tellus, 31, 58-67, doi:10.1111/j.2153-3490.1979.tb00882.x. 1979

Miller, J. B., K. A. Mack, R. Dissly, J. W. C. White, E. J. Dlugokecky, P. P. Tans.: Development of analytical methods and measurements of $^{13}C/^{12}C$ in atmospheric CH_4 from the NOAA Climate Monitoring and Diagnostics Laboratory Global Air Sampling Network, J. Geophys. Res. Atmos. 107, https://doi.org/10.1029/2001JD000630, 2002

Miller, J. B., & Tans, P. P.: Calculating isotopic fractionation from atmospheric measurements at various scales. Tellus Series B Chemical and Physical Meteorology, 55(2), 207–214. https://doi.org/10.1034/j.1600-0889.2003.00020.x, 2003).

Prinn, R. G., J. Huang, R. F. Weiss, D. M. Cunnold, P. J. Fraser, P. G. Simmonds, A. McCulloch, C. Harth, S. Reimann, P. Salameh, S. O'Doherty, R. H. J. Wang, L. W. Porter, B. R. Miller, P. B. Krummel, Evidence for variability of atmospheric hydroxyl radicals over the past quarter century, Geophys. Res. Lett., 32, L078029, 2005

Poirot, R. L., and Wishinski, P. R.: Visibility, sulfate and air-mass history associated with the summertime aerosol in northern Vermont. Atmos. Environ. 20(7), 1457-1469, 1986

Reimann, S., Schaub, D., Stemmler, K., Folini, D., Hill, M., Hofer, P., Buchmann, B., Simmonds, P.G., Greally, B.R., O'Doherty, S.: Halogenated greenhouse gases at the Swiss high alpine site of Jungfraujoch (3580 m asl): continuous measurements and their use for regional European source allocation. J. Geophys. Res. 109, D05307, 2004

Reimann, S., Vollmer, M. K., Folini, D., Steinbacher, M., Hill, M., Buchmann, B., Zander, R., and Mahieu, E.: Observations of long-lived anthropogenic halocarbons at the high-alpine site of Jungfraujoch (Switzerland) for assessment of trends and European sources. Sci. Total Env. 391, 223-231, 2008.

Rella, C. W., Chen, H., Andrews, A. E., Filges, A., Gerbig, C.,Hatakka, J., Karion, A., Miles, N. L., Richardson, S. J., Steinbacher, M., Sweeney, C., Wastine, B., and Zellweger, C.: High accuracy measurements of dry mole

fractions of carbon dioxide and methane in humid air, Atmos. Meas. Tech., 6, 837?860, doi:10.5194/amt-6-837-2013, 2013.

Seibert, P., Kromp-Kolb, H., Baltensperger, U., Jost, D.T., Schwikowski, M., Kasper, A., Puxbaum, H.: Trajectory analysis of aerosol measurements and high alpine sites. In: Borrell, P.M., Cvitai, T., Seiler, W. (Eds.) Transport and transformation of pollutants in the troposphere, pp. 689-693. Academic Publishing, Den Haag,1994

Seo W., H. Lee, Y.-H. Kim, Revision of 22-year Records of Atmospheric Baseline CO2 in South Korea: Application of the WMO X2019 CO2 Scale and a New Baseline Selection Method (NIMS Filter), Atmosphere. Korean Meteorological Society, 31, 5, 1-14, 2021.

Sherwood, O. A., Schwietzke, S., Arling, V. A., & Etiope, G. Global inventory of gas geochemistry data from fossil fuel, microbial and burning sources, version 2017. Earth System Science Data, 9(2), 639–656. https://doi.org/10.5194/essd-9-639-2017, 2017

Thoning K, W., P. P. Tans, and W. D. Komhyr: Atmospheric Carbon dioxide at Mauna Loa Observatory 2. Analysis of the NOAA GMCC Data, 1984-1985. J. Geophys.Res. 8549-8565, 1989

Turnbull, J.C., Rayner, P., Miller, J., Newberger, T., Ciais, P. and Cozic, A.: On the use of $_{14}CO_2$ as a tracer for fossil fuel CO_2: 30 Quantifying uncertainties using an atmospheric transport model, J. Geophys. Res., 114, D22302, https://doi.org/10.1029/2009JD012308, 2009

Turnbull, J. C., Sweeney, C., Karion, A., Newberger, T., Lehman, S. J., Tans, P. P., Davis, K. J., Lauvaux, T., Miles, N. L., Richardson, S. J., Cambaliza, M. O., Shepson, P. B., Gurney, K., Patarasuk, R., and Razlivanoc, I.: Toward quantification and sources sector identification of fossil fuel CO2 emissions from an urban area: Results from the INFLUX experiment, J. Geophys. Res.- Atmos., 120, 292–312, https://doi.org/10.1002/2014JD022555, 2015

Varga, T., R. E. Fisher, J. L. France, L. Haszpra, A. J. T. Jull, D. Lowry, I. Major, M. Molnar, E. G. Nisbet, and E. Laszlo, Identification of Potential Methane Source Regions in Europe Using δ13CCH4 Measurements and Trajectory Modeling, Journal of Geophysical Research: Atmospheres, 126, e2020JD033963. https://doi.org/10.1029/2020JD033963, 2021

Verhulst, K. R., A. Karion, J. Kim, P. K. Salameh, R. F. Keeling, S. Newman, J. Miller, C. Sloop, T. Pongetti, P. Rao, C. Wong, F. M. Hopkins, V. Yadav, R. F. Weiss, R, M. Duren, and C. E. Miller, Carbon dioxide and methane measurements from the Los Angeles Megacity Carbon Project – Part 1: calibration, urban enhancements, and uncertainty estimates, Atmos. Chem. Phys., 17, https://doi.org/10.5194/acp-17-8313-2017, 8313-8341, 2017

Wang, F., S. Maksyutov, R. Janardanan, A. Tsuruta, A. Ito, I. Morino, Y. Yoshida, Y. Tohjima, J. W. Kaiser, G. Janssens-Maenhout, X. Lan, I. Mammarella, J. V. Lavric and T. Matsunaga.: Interannual variability on methane emissions in monsoon Asia derived from GOSAT and surface observations, Environ. Res. Lett., 16, https://doi.org/10.1088/1748-9326/abd352, 2021

Wang, F., S. Maksyutov, R. Janardanan, A. Tsuruta, A. Ito, I. Morino, Y. Yoshida, Y. Tohjima, J. W. Kaiser, X. Lan, Y. Zhang, I. Mammarella, J. V. Lavric, and T. Matsunaga.: Atmospheric observations suggest methane emissions in north-eastern China growing with natural gas use, Sci. Rep., 12:18587, https://doi.org/10.1038/s41598-022-19462-4, 2022

Watanabe, F., O. Uchino, Y. Joo, M. Aono, K. Higashijima, Y. Hirano, K. Tsuboi and K. Suda.: Interannual Variation of Growth Rate of Atmospheric Carbon Dioxide Concentration Observed at the JMA's Three Monitoring Stations:

Large Increase in Concentration of Atmospheric Carbon Dioxide in 1998, J. Meteorol. Soc. Japan., 78(5), 673-682, 2000

Winderlich, J., H. Chen, C. Gerbig, T. Seifert, O. Kolle, J. V. Lavric, C. Kaiser, A. Höfer, and M. Heimann.: Continuous low-maintenance CO2/CH4/H2O measurements at the Zotino Tall Tower Observatory (ZOTTO) in Central Siberia, Atmos. Meas. Tech., 3, 1113-1128, 2010

WMO: Greenhouse Gas Bulletin, The State of Greenhouse Gases in the Atmosphere Based on Global Observations through 2020, No.17, 25 October 2021

Worthy, D. E. J., I. Levin, N. B. A. Trivett, A. J. K. Kuhlmann, J. F. Hopper, and M. K. Ernst.: Seven years of continuous methane observations at a remote boreal site in Ontario, Canada, J. Geophys. Res., 103(D13), 15995–16007, doi:10.1029/98JD00925., 1998

Zhao, Cong Long and Tans, Pieter P. : Estimating uncertainty of the WMO mole fraction scale for carbon dioxide in air. Journal of Geophysical Research, 111, D08S09, doi:10.1029/2005JD006003, 2006

Zhou, L. X., D. E. J. Worthy, P. M. Lang, M. K. Ernst, X. C. Zhang, Y. P. Wen, and J. L. Li (2004), Ten years of atmospheric methane observations at a high elevation site in Western China, Atmos. Environ., 38(40), 7041–7054, doi:10.1016/J.atmosenv.2004.02.072.

Zhang F., L.-X. Zhou, L. Xu, Temporal variation of atmospheric CH4 and the potential source regions at Waliguan, China, Earth Sciences, 56, 727–736, doi: 10.1007/s11430-012-4577-y, 2013

Zhang, X., Hong Jiang , Yueqi Wang , Ying Han , M. Buchwitz ,O. Schneising & J. P. Burrows, Spatial variations of atmospheric methane concentrations in China, International Journal of Remote Sensing, 32:3, 833-847, DOI:10.1080/01431161.2010.517804, 2011